MIT Open Access Articles

Orbital Equivalence of Terrestrial Radiation Tolerance Experiments

Orbital Equivalence of Terrestrial Radiation Tolerance Experiments

Julie V. Logan, Michael P. Short, Preston T. Webster, and Christian P. Morath

Abstract—High energy (>40 MeV) protons are commonly used to characterize space electronics' radiation tolerance against damage caused by energy transfer to the nuclei and electrons of semiconductor materials while in orbit. While practically useful, these experiments are unrepresentative in terms of particle type and energy spectra, which results in disproportionate amounts of displacement damage and total ionizing dose. We compare these damages to those realized by bulk semiconductors used in optoelectronics in common low, medium, and high Earth orbits by calculating the duration in orbit required to achieve equivalent nuclear and electronic energy deposition. We conduct this analysis as a function of test proton energy, material, material thickness, and shielding thickness. The ratio of nuclear to electronic orbit duration, a value which would approach unity in an ideal radiation tolerance test, is found to exceed unity in the majority of cases but approaches unity as Al shielding increases. This study provides a connection between damage produced in terrestrial accelerator-based characterizations and orbit irradiation in terms of both damage modes which can cause optoelectronic components to fail: displacement damage and total ionizing dose.

Index Terms—semiconductors, radiation tolerance, orbit environment, space weather

I. INTRODUCTION

OVER 50% of spacecraft equipment malfunctions are caused by the cosmic environment, with the majority of these resulting from radiation damage to critical components [1]. This necessitates the usage of radiation-hardened components, which themselves drive the cost of space missions largely due to long lead times and low demand [2]. Long engineering design cycles and low performance with respect to the terrestrial state of the art are direct results of this additional requirement. Radiation-hardened components are generally 10 years behind the cutting edge in sophistication due to the need to characterize components and devices to high radiation doses (over 100 krad), and the scarcity of facilities to perform this testing. An alternative approach focuses on evaluation of commercial, off-the-shelf components tested and found to function to a specified dose level. While most commercial components are radiation tolerant up to a dose of 5 krad, some

will fail before 1 krad of dose is reached, and this cannot be known *a priori* [2], [3].

In practice, this testing is executed using gamma photon (^{60}Co), proton, and heavy ion experiments. Gamma rays produce ionization, but do not produce substantial displacement damage and have too low a linear energy transfer (LET) to produce single event effects. Heavy ions, on the other hand, can be accelerated so as to have sufficient LET to simulate the full range of the radiation environment effects [2], [4], but these tests have low availability. Alternatively, proton sources with energies above ∼40 MeV provide an excellent compromise and are used to test total dose and displacement damage effects, as well as single event upset, single event functional interrupt, and to screen for unacceptably low threshold single event latchup, single event burnout, and single event gate rupture effects. [2] Both displacement damage and total ionizing dose have been studied extensively in the literature through both modeling and experiments in semiconductors [5]–[9].

In this study, we analyze how well terrestrial proton irradiation facilities can simulate the full extent of radiation damage incurred by satellites in seven common Earth orbits. It should be emphasized that the damage referred to in this analysis is the initial energy deposited and does not incorporate the complex material-specific defect recovery processes which follow. We compare the amounts of damage incurred by electronic (total ionizing dose) and nuclear (displacement damage) modes in orbit and in terrestrial characterization to determine the required fluence for a particular proton energy to replicate an equivalent time-in-orbit for each semiconductor, at each orbit under consideration, for each damage mode. These results are obtained as a function of material thickness, Al shielding thickness, and orbit. The results are of specific applicability to bulk materials and we focus on the following semiconductors of interest to optoelectronic devices: Si, MgO, ZnO, InAs, InP, GaP, GaN, $Hg_{0.5}Cd_{0.5}Te$, $In_{0.5}Ga_{0.5}Sb$, $In_{0.5}Ga_{0.5}As$, ZnTe, ZnSe, ZnS, CdTe, and InSb. Heterostructures and CMOS architectures are not analyzed, although general material-independent derived trends can be extrapolated. The results of this study provide a connection between damage produced in terrestrial accelerator-based characterizations and orbit irradiation in terms of both damage modes which can cause optoelectronic components to fail: nuclear and electronic energy deposition. The ratio of a test's nuclear to electronic equivalent duration is also analyzed. This ratio would ideally be unity, implying that the nuclear and electronic energy deposition are proportional to that experienced in orbit. This is important because electronic energy loss has been shown

to permit radiation-enhanced or radiation-induced diffusion in semiconductors, allowing displaced atoms to regain their initial lattice position. Thus, if the electronic energy loss is unproportionally high, the displacement damage realized may be unproportionally low, even if an accurate dose is applied. [10]–[13] It should be noted that the intent of this study is to provide a general early assessment of dose for the purpose of characterization of radiation tolerance of novel optoelectronic materials and device architectures. Prior to use of a component in a mission, the specific mission dose (accounting for particular anticipated shielding) would be carefully assessed to calculate the fluence required to achieve the specific orbit duration called for [7], [8], [14], [15]. It is general knowledge that monoenergetic, normally-incident proton ground-testing cannot match both the displacement damage and total ionizing dose in orbit. This paper demonstrates the magnitude of this mismatch and how this mismatch varies with proton energy used in characterization, Al shielding thickness, orbit, and bulk material.

II. Background

A. Effects of Space Radiation on Semiconductors

Materials in space incur radiation damage through electronic (ionizing and charge transfer) effects as well as nuclear displacement damage. Charged particles lose energy electronically via the excitation of electron-hole pairs by ionization in materials. Charge transfer effects lead to stationary and non-stationary currents, resulting in surface and volume charge accumulation in dielectrics [16], [17]. Displacement damage results from the transfer of sufficient energy to lattice atoms by incident energetic particles to force them out of their prior lattice position. The effect of this displacement damage on semiconductor electrical and optical properties stems fundamentally from the introduction of energy levels within the bandgap. These levels result in reduction of carrier recombination lifetime, diffusion length, and generation lifetime; increase in carrier trapping, thermal generation, and tunneling; and change in carrier concentrations [1], [18], [19].

The fluxes and energy spectra of particles encountered in a particular orbit determine the rate and extent of component degradation due to space radiation. Differences in the local cosmic environment as they pertain to damaging critical optoelectronic and microelectronic components can be separated into those originating inside or outside the Earth's magnetosphere, which extends 6×10^4 km in the direction of the Sun and 2-2.5×10^5 km in the transverse dimension along the meridian plane. Inside the Earth's magnetosphere, the most prevalent damaging particles are relatively low energy protons and electrons trapped in the Earth's radiation belts. The majority of protons fall in the 1–30 MeV range, while the majority of electrons have energies of 0.1–1 MeV. Outside the magnetosphere, far higher energy solar cosmic rays (SCRs) and galactic cosmic rays (GCRs) are dominant. SCRs are primarily composed of protons emitted from intense solar eruptions with energies of 1-10^4 MeV. GCRs are isotropic, originating from regions dispersed throughout the galaxy, and consist of 100-10^{14} MeV protons and heavier nuclei [1].

TABLE I
PROTON TEST ENERGIES USED IN EQUIVALENCE CALCULATIONS. THESE CONSTITUTE THE MAXIMUM PROTON ENERGIES AVAILABLE AT THE PRIMARY NORTH AMERICAN FACILITIES PERFORMING PROTON COMPONENT TESTS FOR SPACE APPLICATIONS [2], [20], [21].

Max Test Proton Energy [MeV]	Facility
45	Texas A&M University
55	Lawrence Berkeley National Laboratory
63	University of California at Davis
230	Francis H. Burr Proton Therapy Center
500	TRIUMF, Vancouver
2500	NASA Space Radiation Laboratory

B. Terrestrial Proton-Based Tests to Replicate Space Radiation at Different Orbits

The main North American facilities performing proton component tests to simulate these cosmic environments use energies up to 45–2500 MeV, as shown in Table I [2], [20]–[32]. The use of these high energies serves two purposes. First, they deliver approximately uniform energy deposition in a component, minimizing spatial non-uniformity effects of the test. Second, they improve the probability of producing some high LET particles in the active region of a component through displacement damage, in which a lattice atom is accelerated through the proton impact [2]. With a specific damage mechanism in mind, the nuclear and electronic proton test energy deposition must be connected to the nuclear and electronic energy deposition expected in space.

There are three categories of useful satellite orbits: high Earth orbit (HEO), medium Earth orbit (MEO), and low Earth orbit (LEO), with altitudes (relative to the Earth's surface) of $\geq$ 35,780 km, 2,000–35,780 km, and 160–2,000 km respectively. Also important in the orbit definition is its inclination (orbit angle relative to the equator) and eccentricity (deviation from circular orbit measured on a scale from 0 to 1) [33], [34].

HEO satellites are typically used for Earth, solar, and space weather monitoring and communication. One important HEO orbit is the geostationary orbit (GEO), which occurs when a satellite matches Earth's rotation, rotating at the same speed and maintaining the same longitude at all times. This is useful for weather monitoring and communication because a consistent view of the same area is maintained [34]–[36]. MEO orbits are well-suited for navigation, communication, and for monitoring of a particular region of Earth. Two relevant MEO orbits are the Molniya orbit and the semi-synchronous global positioning system (GPS) orbit, both of which match Earth's rotation rate and follow the same path every 24 hours. The Molniya orbit is optimized for high latitude sensing and communication through its high inclination and high eccentricity, while the GPS orbit has zero eccentricity for better Earth-positional accuracy [37], [38]. Most scientific satellites take on a low eccentricity LEO, with the inclination dependent upon the satellite's particular mission. These altitudes require the least power to communicate with Earth. Here, observational instruments have maximum resolution, with many of these Earth observing satellites having high inclination orbits to permit polar visibility, such as the polar Sun-synchronous

orbits. The International Space Station (ISS) also follows a LEO to minimize astronaut travel time and energy required to fly resupply loads to the station as well as to reduce the radiation effects which would be experienced in MEO [33], [34].

III. METHODS

A. Data on Orbits and Their Cosmic Environments

A summary of the altitude, inclination, and eccentricity of the orbits considered in this analysis is given in Table II, while the energy spectra of particles for these seven common Earth orbits are plotted in Fig. 1 [36], [39]. The nuclear and electronic stopping powers for these particles are plotted in Fig. 2a and Fig. 2b respectively in Si as a reference material [40]–[43].

The orbit radiation flux energy spectra are obtained using the SPace ENVironment Information System (SPENVIS) maintained by the European Space Agency [36]. The European Cooperation for Space Standardization standard models are used for each radiation source [33]. The Van Allen belt trapped proton and electron spectra are obtained from the solar minimum AP-8 model [44] and solar maximum AE-8 model respectively [45]. These solar conditions maximize the radiation environment and, as such, will yield a worst-case estimate of the radiation-induced damage. The ESP-PSYCHIC (total fluence) model, accounting for magnetic shielding, is employed to obtain solar proton and He spectra, with a confidence level of 50% [46]. The 50% confidence level is representative of the average solar particle fluence over a satellite lifetime [39]. The inclusion of just H and He is sufficient because these two particles constitute 99% of the solar particle dose (with protons causing 90% and He depositing 9%) [39]. GCR spectra are obtained from the mission epoch ISO-15390 model with magnetic shielding. Among GCR, all particles whose abundance at any point in the spectrum exceeds 1% of that of GCR protons are considered for model inclusion: these include He, C, N, O, Ne, Mg, Si, and Fe [47]. Only GCR H is shown to contribute substantially and to merit inclusion in the model, as shown in Appendix A.

For both solar and GCR magnetic shielding, an omnidirectional, quiet magnetosphere is accounted for using the Stormer eccentric dipole model without an alteration to the magnetic field moment. When a solar flare occurs, a magnetic storm on Earth is usually triggered. A quiet magnetosphere model assumes that these storms are not occurring [36].

The orbital spectra obtained following traversal of the spectrum through 0.1, 0.5, 1.0, 2.0, and 5.0 g/cm^2 thicknesses of Al shielding (0.037-1.9 cm thick) are also used in calculation of equivalences. As SPENVIS models are not available for the Al shielded solar He and GCR H spectra, GEANT4 simulations are employed to obtain said spectra, as discussed in Appendix B. High energy protons also have the potential to interact with this Al shielding and produce neutrons. In Appendix C, it is shown that the neutron dose fraction for the maximum neutron fluence orbit (5.0 g/cm^2 Al shielding, LEO polar Sun-synchronous 800 km orbit) does not exceed 6% of the total dose and can be neglected in this analysis because it is

eclipsed by the uncertainties in the model spectra themselves, which are at best a factor of 2-3 for trapped radiation and higher for the solar and GCR spectra [33].

The nuclear stopping power tables for all materials and all particles (electrons and ions) are obtained from the L'Istituto Nazionale di Fisica Nucleare (INFN) Screened Relativistic Non-Ionizing Energy Loss (SR-NIEL) Nuclear Stopping Power models [40]. The electronic stopping power for ions is obtained from SRIM 2013 with the high energy extension from Leroy and Rancoita as implemented by SR-NIEL [41], [42]. The electronic stopping power for electrons comes from the NIST ESTAR database [43]. All tables are obtained to cover the entire SPENVIS orbital spectral range. The damage produced through inelastic nuclear reactions is negligible in comparison to that caused by displacement damage, as indicated by the NIEL [48]. As discussed in Section I, electronic and nuclear energy loss are important in producing damage in different applications. For this reason, nuclear and electronic equivalences are computed separately.

Given the discretized orbital energy spectra for each particle type in each orbit, radiation from each energy bin is propagated through each material to a maximum depth of 2.0 mm. The distance step size of 0.1 μm is employed, to ensure that the sharp Bragg peak near the end of the ion range is properly captured in the spatial discretization. Any errors due to depth discretization will not impact total energy deposition because the total energy is deposited in the final step if the particle's energy drops below the stopping power table minimum. Any errors due to the discretized orbital energy spectra are analyzed in Appendix D by increasing the number of flux energy bins by an order of magnitude. The resulting dose impact is shown to never exceed 6%, which is eclipsed by the minimum factor of 2–3 error in the flux spectra themselves [33].

The total nuclear energy loss, electronic energy loss, and average particle energy in each step is recorded every 1 μm (every 10 computation steps) and the results are written to file every 10 microns (every 100 computation steps). This computation provides, for each particle spectral energy bin and each material, the nuclear and electronic energy loss as a function of depth into the material. For each orbit spectrum, the sum of these values, as weighted by the flux in that energy bin, is accumulated. This provides the nuclear and electronic energy deposited per unit time as a function of distance into each material for each orbit, as given by $P_0^e(x)$ in (1) for electronic energy deposition. The spatial distribution of the spectra is taken as isotropic, which gives a cumulative distribution function of incident angle with respect to the sample normal of $\sin^{-1}([0, 1]^{1/2})$ where $[0, 1]$ represents random uniform sampling from 0 to 1. All particle deposited energies are projected according to this distribution to reflect the truly isotropic radiation environment of space [49]. The total nuclear and electronic energy loss in the depth range of interest is summed to obtain the energy deposition rate in orbit for a particular sample thickness.

An analogous calculation is done for the monoenergetic accelerator-based test energies at a given test fluence to obtain the nuclear and electronic energy deposited in the test as a function of depth, the latter given by $E_t^e(x)$. When this test
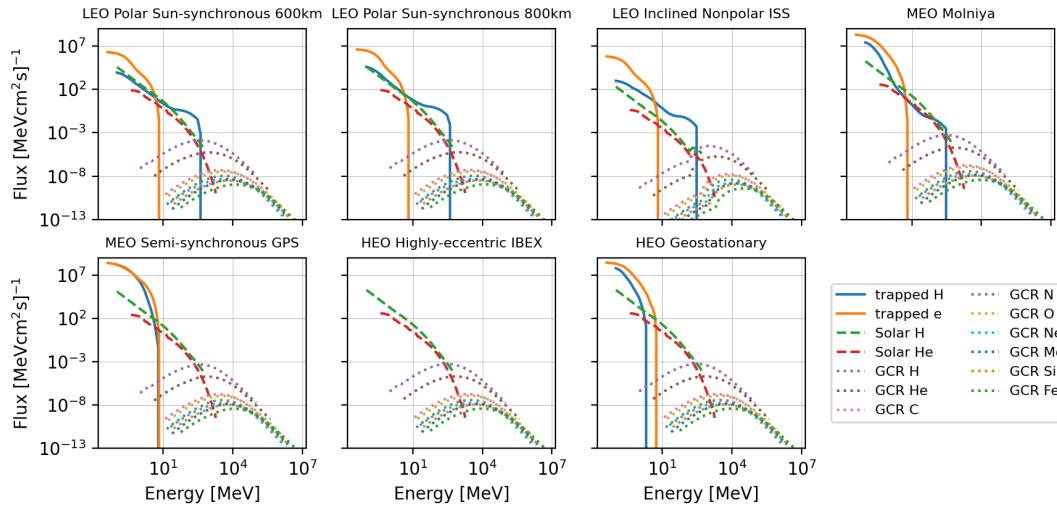
Fig. 1. Flux spectra of all particles and orbits considered in this study, including trapped protons and electrons, solar H and He (which constitute 99% of the solar dose), and the dominant galactic cosmic ray (GCR) ions (H, He, C, N, O, Ne, Mg, Si, and Fe) [36], [39].

TABLE II
DETAILS OF ORBITS CONSIDERED IN THIS ANALYSIS. ALTITUDE IS GIVEN AS APOGEE/PEROGEE (IN ADDITION TO THE SEMI-MAJOR AXIS (SEMI-A))
[33]–[38].

Orbit	Altitude [km]	Inclination	Eccentricity [frac]
LEO Polar Sun-synchronous (LOW)	600	97.79°	0
LEO Polar Sun-synchronous (HIGH)	800	98.6°	0
LEO Inclined Non-polar (ISS)	400	51.6°	0
MEO Molniya	545/39,913 (Semi-A 26,600)	63.4°	0.74
MEO Semi-synchronous (GPS)	20,200	55°	0
HEO High-eccentricity (IBEX)	9,566/302,936 (Semi-A 162,622)	24.2°	0.902
HEO Geostationary	35,793	0°	0

energy deposited is summed for the sample thickness and divided by the orbit energy deposition rate $\left[\frac{\text{MeV/cm}^2}{\text{MeV/cm}^2\text{s}}\right]$, one obtains the equivalent time in a particular orbit associated with a given test, as shown in (1) for electronic energy deposited equivalence.

$$\frac{\sum\limits_{0}^{x_m} E_t^e(x)}{\sum\limits_{0}^{x_m} P_o^e(x)} = \frac{\Phi_t \sum\limits_{0}^{x_m}\left[\frac{dE^e(E_t(x))}{dx}dx\right]}{\sum\limits_{0}^{x_m}\sum\limits_{p}\left[\sum\limits_{i}\varphi_{pi}\frac{dE_p^e(E_i(x))}{dx}dx\right]} = \Phi_t M(x_m) \quad (1)$$

in which x_m is the material thickness of interest, $E_t^e(x)$ is the total test electronic energy deposited per unit distance, $P_o^e(x)$ is the total orbit electronic energy deposition rate per unit distance, Φ_t is the test proton fluence, φ_{pi} is the flux for the orbit flux energy bin i and particle p, and $\frac{dE_p^e(E_i(x))}{dx}$ is the electronic stopping power of particle p of incident bin energy of E_i at its energy at depth x into the material. This relation is linear with respect to test fluence for a particular orbit, test energy, material thickness, and Al shielding combination (slope of $M(x_m)$). An analogous computation is performed for nuclear energy deposition.

The test energies E_t included in the analysis are 45, 63,

100, 200, and 230 MeV. The materials included are Si, MgO, ZnO, InAs, InP, GaP, GaN, $Hg_{0.5}Cd_{0.5}Te$, $In_{0.5}Ga_{0.5}Sb$, $In_{0.5}Ga_{0.5}As$, ZnTe, ZnSe, ZnS, CdTe, and InSb. The material determines both the test and orbit nuclear and electronic stopping powers used in (1).

All datasets (orbit radiation environments and particle stopping powers) as well as analysis files are available in the GitHub repository published with this work [50].

IV. RESULTS

The increase in equivalent time in orbit (nuclear and electronic) per additional 10^{11} p/cm^2 test fluence is shown in Fig. 3. This orbit time per test fluence (OTTF) slope represents the linear scaling of proton test dose with fluence, as shown in (1). Nuclear equivalence (top row) and electronic equivalence (bottom row) are shown as a function of material thickness for different Al shielding thicknesses (columns) of unshielded, 0.5 g/cm^2, and 5 g/cm^2. The shaded regions show the standard deviation in the data, caused by the fact that all materials and all test energies (Table I) are included in the plotted data.

As the material thickness increases, the OTTF slope increases nonlinearly due to the fact that the orbit energy deposition is skewed toward lower thicknesses (both due to the isotropic nature of the orbit irradiation as well as the
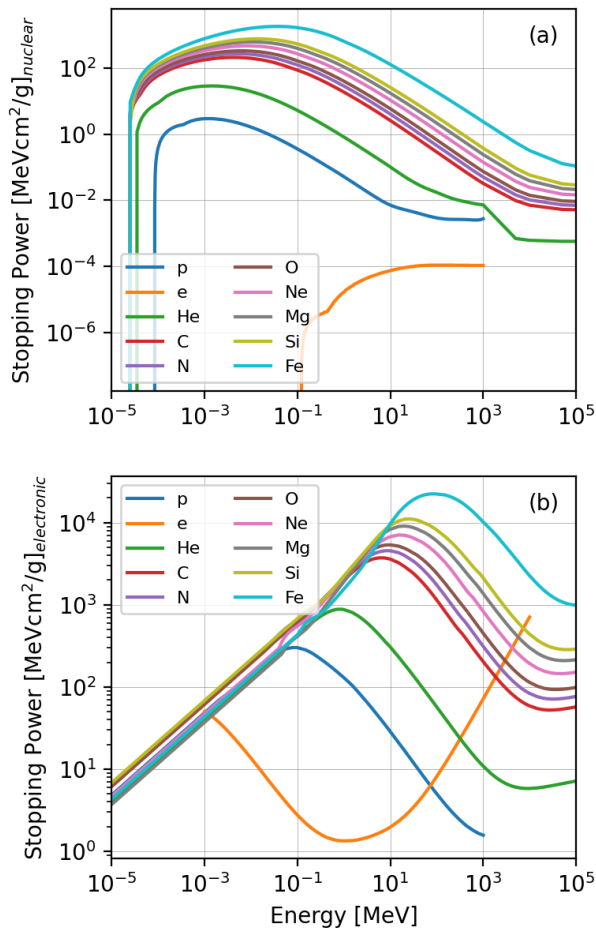
Fig. 2.   Nuclear (a) and electronic (b) mass stopping power for electrons and all relevant ions in Si as a reference material [40]–[43].

LEO polar Sun-synchronous orbits decrease in the orbit OTTF slope ranking as a function of Al shielding thickness because they have trapped spectra which extend to higher energies that are not effectively shielded. These continue to contribute to the denominator of (1), keeping the OTTF slope low as shielding thickness increases.

The OTTF slope for nuclear (left) and electronic (right) equivalence is shown as a function of test energy in Fig. 4 for all materials and material thicknesses at 1.0 g/cm^2 Al shielding. The bars represent the quartiles (caused by material and material thickness OTTF variation) and the whiskers extend a factor of 1.5 above and below the interquartile range. The OTTF slope decreases as test energy increases because higher energy test protons deposit less energy into the material, as shown in Fig. 2, which decreases the numerator of (1). More outliers are observed at the higher OTTF range. This is explained by the approximate exponential relationship between OTTF slope and material thickness, as shown in Fig. 3.

To best represent the true orbit damage conditions, one should perform a test with the proper orbit equivalent duration in terms of both nuclear and electronic energy deposited. For this to be so, the ratio of the nuclear to electronic equivalent duration given by (2) should be unity so that the required duration can be controlled by test fluence alone. It is equal to the ratio of the equivalent time in orbit for a given test energy and sample thickness for nuclear and electronic energy deposition.

$$\frac{\sum_{0}^{x_m} E_t^n(x) \Big/ \sum_{0}^{x_m} P_o^n(x)}{\sum_{0}^{x_m} E_t^e(x) \Big/ \sum_{0}^{x_m} P_o^e(x)} = \left[\frac{\sum_{0}^{x_m} E_t^n(x)}{\sum_{0}^{x_m} E_t^e(x)}\right]\left[\frac{\sum_{0}^{x_m} P_o^n(x)}{\sum_{0}^{x_m} P_o^e(x)}\right]^{-1} \quad (2)$$

The ratio of nuclear to electronic orbit duration equivalence as a function of material thickness, with spread due to inclusion of all test energies and all materials, is plotted for four Al shielding thicknesses (unshielded, 0.5 g/cm^2, 1 g/cm^2, and 5 g/cm^2) in Fig. 5. This quantity is independent of test fluence, as shown in (2). The ratio is most commonly greater than unity, which indicates that either the total nuclear energy loss of test protons is greater than their electronic energy loss or that the electronic energy loss rate of the particles in orbit is greater than their nuclear energy loss rate. However, the former cannot be true as the ratio of proton nuclear to electronic stopping power plotted as a function of proton energy in Fig. 6 never exceeds unity. As a result, test proton nuclear energy deposition cannot exceed electronic energy deposition. The latter, that orbit electronic energy loss rate exceeds that of orbit nuclear energy loss, is very likely to be true as is also observed in Fig. 6. This explains the dominance of nuclear to electronic orbit duration equivalence ratios which exceed unity.

With the exception of the LEO orbits, the ratio of nuclear to electronic equivalence in Fig. 5 first increases as Al shielding is introduced and then decreases thereafter as Al shielding thickness further increases. As a function of Al shielding, the average proton energy for these non-LEO orbits increases from

lower energy orbit spectra) while the test energy deposition is uniformly distributed through the material due to the exclusive use of high energy protons in the test. This being the case, as thickness increases, test energy deposited increases at a greater rate than does orbit energy deposited, which increases the ratio in (1) nonlinearly. This trend is most prominant for the low Al shielded cases because these orbit spectra maintain more of their low energy, high stopping power particles.

The MEO semi-synchronous GPS and HEO geostationary orbits have the smallest OTTF slope for the no shielding case in both nuclear and electronic equivalence, but both increase more quickly than the other orbits as a function of Al thickness and become the largest as Al shielding increases to 5 g/cm^2. This is explained by the large flux of low energy trapped protons for these orbits, as visualized in Fig. 1, which are effectively shielded as Al shielding increases. MEO Molniya orbit also has this large flux of low energy particles and follows a similar trend as a function of Al shielding. The LEO inclined nonpolar ISS and HEO highly-eccentric IBEX orbits remain amongst the largest in terms of OTTF slope for both nuclear and electronic equivalence for all Al shielding thicknesses. This is due to the lower fluences for trapped, solar, and GCR sources for these orbits, as shown in Fig. 1. Both
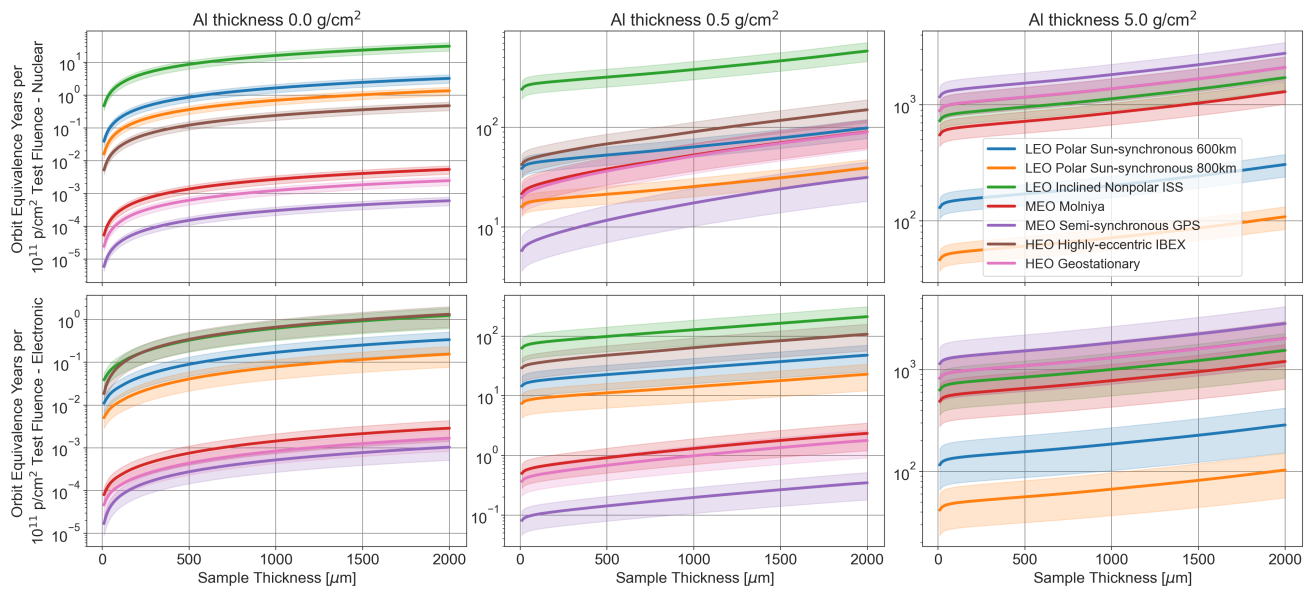
Fig. 3. Orbit time per test fluence (OTTF) slope for nuclear (top) and electronic (bottom) equivalence as a function of material thickness, with columns representing different Al shielding levels (unshielded, 0.5 g/cm², 5 g/cm²). The shaded regions represent the standard deviation, resulting from inclusion of all materials and all test energies (Table I) in the plot. There is a nonlinear increase with material thickness. The trends in the relative ranking of orbits as a function of shielding thickness depend on the details of the orbit spectra, shown in Fig. 1.
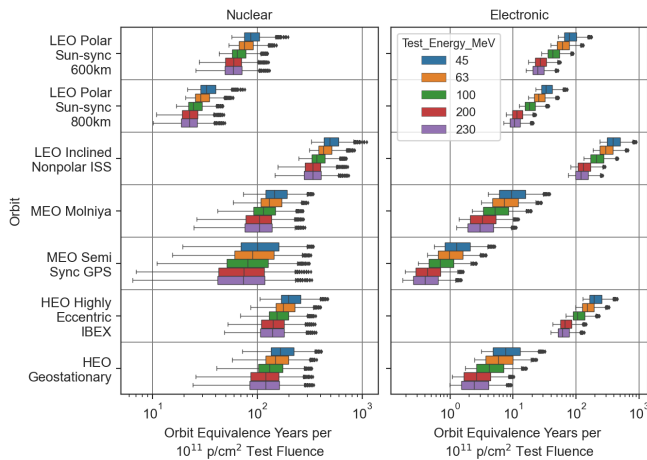

Fig. 4. Orbit time per test fluence (OTTF) slope for nuclear (left) and electronic (right) equivalence for all test energies at 1.0 g/cm² Al shielding thickness for all materials and material thicknesses. The bars represent the quartiles and the whiskers extend a factor of 1.5 above the interquartile range. The orbital equivalence decreases as test energy increases.
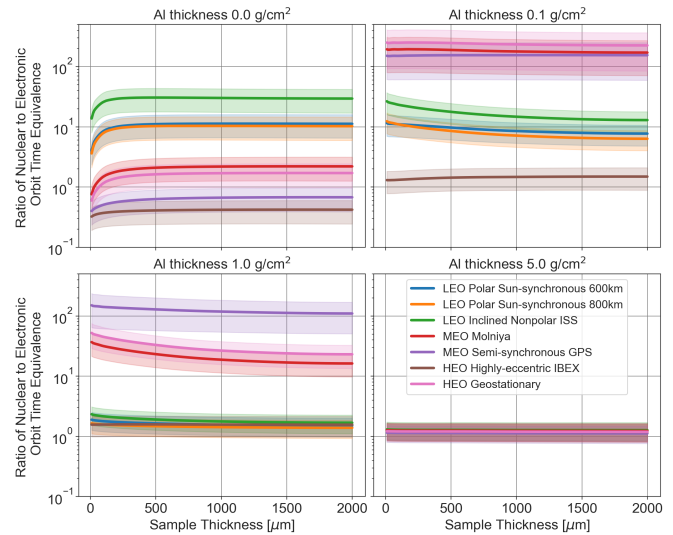

Fig. 5. Ratio of nuclear to electronic test equivalent orbit duration for a subset of shielding thicknesses (unshielded, 0.1 g/cm², 1 g/cm², and 5 g/cm²) as a function of material thickness for all orbits. This quantity is independent of test fluence. The shaded regions represent the standard deviation, resulting from inclusion of all materials and all test energies (Table I) in the plot. The ratio generally exceeds unity, but approaches unity as Al shielding thickness increases. Non-LEO orbits achieve their maximum ratio at intermediate Al shielding while LEO orbits achieve their maximum ratio with no Al shielding.

~0.015 to ~40 MeV. Through this progression, the nuclear to electronic stopping power ratio in Fig. 6 first decreases then increases. This results in a decrease then increase in the orbit energy deposition ratio term of (2), which causes the nuclear to electronic orbit duration ratio to increase and then decrease as a function of Al shielding as is observed in Fig. 5. In the case of the LEO orbits, the average proton energy increases from ~0.025 to ~50 MeV as a function of Al shielding. In this case, the nuclear to electronic stopping power ratio primarily increases, resulting in decreasing ratio of nuclear to electronic equivalent duration. For all orbits, as the Al shielding increases, the orbit duration ratio becomes closer

to unity as the lower energy particles are absorbed within the Al shielding and only the high energy orbit particles can make it through to the material. At this point, the orbit spectrum becomes more similar to the test spectrum and represents a similar ratio of nuclear to electronic stopping power. This is ideal for a testing perspective, but is not in control of the experimenter because the Al shielding thickness is constrained to that which is actually used in the satellite. The experimenter
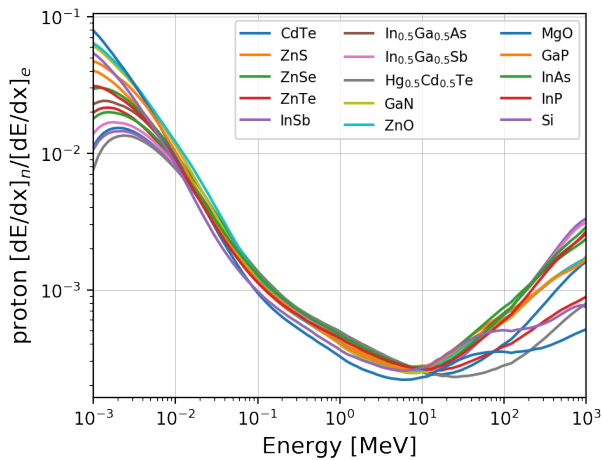
Fig. 6. Ratio of proton nuclear to electronic stopping power as a function of energy for all materials considered in this analysis. The nuclear stopping power never exceeds the electronic stopping power, indicating that proton electronic energy loss will always exceed nuclear energy loss.

does have control over the proton test energy. It is observed that the higher the test energy, the larger the test nuclear to electronic energy deposition ratio, as is observed in Fig. 6. This increases the nuclear to electronic test equivalent duration ratio as a function of test energy through the first term in (2). As such, for low-shielding cases, one should use lower energy test protons to bring the nuclear and electronic energy deposition orbit durations together. If a characterization highly values achieving precise displacement damage and total ionizing dose, these can be controlled approximately independently employing neutrons and gamma or x-ray ray photons respectively [18], [51]. It should be recognized, though, that simultaneous nuclear and electronic equivalence is not always the dominant criterion for selection of proton test energy. For example, high energy protons are often selected to gain insights into single event effects [2], [4].

The LEO orbits have the highest nuclear to electronic orbit duration ratios in the unshielded case. This is explained by the fact that the average proton energies of these orbits fall around the minimum of the nuclear to electronic stopping power ratio in Fig. 6 which, per (2), yields a maximum nuclear to electronic orbit duration ratio. The non-LEO orbits achieve these minimum nuclear to electronic stopping power ratios at intermediate Al shielding thickness and, as such, demonstrate maximum nuclear to electronic orbit duration ratios at higher shielding thicknesses.

In the no-shielding case, the orbit equivalence duration ratio increases with thickness. At shallow depths, low energy orbit particles with a large nuclear to electronic stopping power ratio deposit their energy, which reduces the nuclear to electronic orbit duration ratio per (2). The nuclear to electronic stopping power ratio decreases and the orbit duration ratio increases as the average penetrating radiation spectrum increases in energy with depth. This equivalence depth dependence on active material thickness should be considered in component test design.

There exist additional useful conclusions that can be drawn

from this analysis. First, the error bars in Fig. 3 and 5 show that the material and test energy in the range considered have smaller effect on equivalent orbit duration than do orbit, material thickness, and Al shielding thickness. From these results, one can conclude that the equivalent durations can be roughly extrapolated to materials of similar density outside the scope of our analysis and interpolated for test energies not directly assessed. Furthermore, the results of this analysis provide an estimate of error associated with testing under uncharacteristic Al shielding thickness or material thickness.

V. CONCLUSION

It is general knowledge that monoenergetic, normally-incident proton ground-testing cannot match both the displacement damage and total ionizing dose induced in the complicated radiation environment of orbit. We have shown the magnitude of this mismatch as a function of test proton energy, Al shielding thickness, bulk material, and material thickness. This analysis was conducted for materials of interest for optoelectronic applications, but the general trends are shown to be weakly dependent upon material in comparison to the other variables analyzed. Furthermore, the methodology presented could be expanded to other bulk materials not specifically analyzed. The ratio of nuclear to electronic orbit duration, a value which would approach unity in an ideal radiation tolerance test, is found to exceed unity in the majority of cases but approaches unity as Al shielding increases. This ratio can be brought to a more ideal value near unity by using lower energy characterization protons for lower Al shielding thicknesses. We connect damage produced in terrestrial accelerator-based characterizations and orbit irradiation in terms of both damage modes which can cause optoelectronic components to fail: displacement damage and total ionizing dose.

APPENDICES

APPENDIX A
ION SIGNIFICANT DOSE CONTRIBUTION DETERMINATION

Despite the fact that SPENVIS ignores the contribution of solar and GCR ions to the shielded dose (except for solar H), we wanted to verify that no other ions contributed significantly for our application. For this reason, in the unshielded case, the orbit duration equivalence is calculated (1) with the inclusion of no $Z > 1$ ions (only trapped protons and electrons and solar protons included), (2) with the inclusion of trapped protons and electrons, solar protons and He, and GCR H, and (3) with the inclusion of all significant ions visualized in Fig. 1. The results are compared in Fig. 7, for the nuclear and electronic energy deposition (top and bottom respectively). It is shown that there is substantial orbit duration difference between the analysis including no $Z > 1$ ions and that including all significant ions, but that there is negligible difference between that including trapped protons and electrons, solar protons and He, and GCR protons and that including all significant ions. This shows that the inclusion of trapped protons and electrons, solar protons and He, and GCR H is sufficient for accurate results.
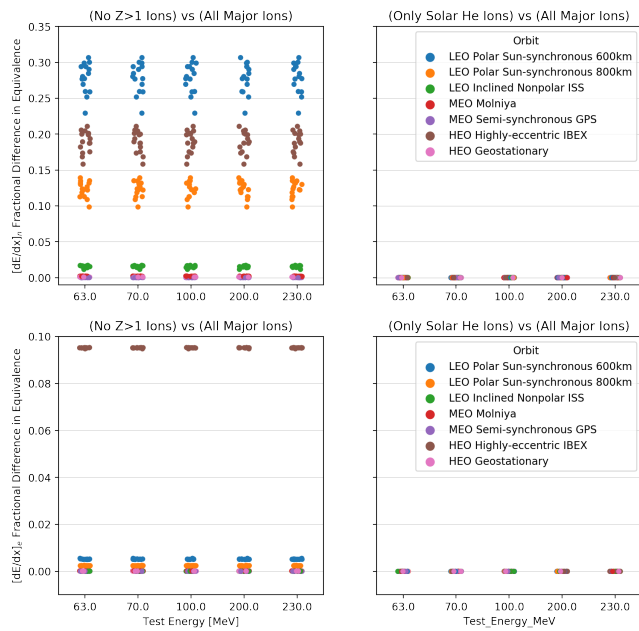
Fig. 7. Fractional difference between the orbit equivalent duration according to nuclear (top) and electronic (bottom) energy loss with reference to the case when all significant Z > 1 ions are included in comparison to that when no ions are included (left) and when only trapped protons and electrons, solar protons and He, and GCR protons are included (right) for 500 μm thickness of all materials considered. This shows that the inclusion of all other significant Z > 1 ions does not contribute substantially to the nuclear or electronic dose and can be excluded. This conclusion is reached independent of material thickness, but the results for 500 μm thickness are visualized for figure clarity.

APPENDIX B
GEANT4 CALCULATION OF AL SHIELDED SPECTRA FOR SIGNIFICANT IONS

In Appendix A, it was determined that the significant ion contributors not automatically included in the shielded SPENVIS calculations are: solar He and galactic H. GEANT4 simulations were used to calculate the energy spectra for each orbit as a function of Al thickness (0.1, 0.5, 1.0, 2.0, and 5.0 g/cm^2). 1,000,000 GCR protons and 5,000,000 fully ionized solar He atoms, the spectra of which is shown in Fig. 1, were simulated. The resulting shielded energy spectra are shown in Fig. 8 and Fig. 9 respectively. These shielded spectra are used as input for the propagation of these particles for each orbit through each material to contribute to the total electronic and nuclear doses.

APPENDIX C
NEUTRON SIGNIFICANT DOSE CONTRIBUTION DETERMINATION

As the thickness of Al shielding increases, the likelihood of a high energy proton undergoing a nuclear reaction which results in the emission of neutron(s) increases. In this section, we analyze the significance of the contribution of these neutrons to the total material dose. This is done for the worst case neutron spectrum considered in this analysis: maximum Al thickness of 5.0 g/cm^2, LEO polar sun-synchronous 800 km orbit, and maximum density material ZnTe at maximum thickness
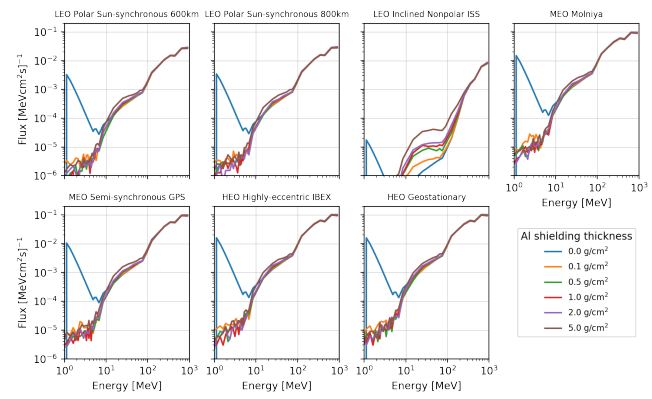

Fig. 8. Energy spectra for GCR protons passing through 0.0 (unshielded), 0.1, 0.5, 1.0, 2.0, and 5.0 g/cm^2 thicknesses of Al shielding for each orbit under consideration. These spectra serve as input to the dose calculation conducted in the main paper because these ions are deemed to contribute non-negligibly to the total dose.
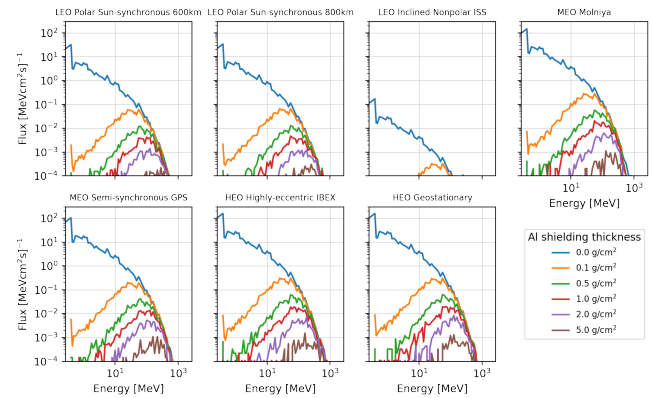

Fig. 9. Energy spectra for solar He ions passing through 0.0 (unshielded), 0.1, 0.5, 1.0, 2.0, and 5.0 g/cm^2 thicknesses of Al shielding for each orbit under consideration. These spectra serve as input to the dose calculation conducted in the main paper because these ions are deemed to contribute non-negligibly.

2.0 mm. The spectrum of these neutrons, as generated by SPENVIS, is shown in Fig. 10.

30,000,000 neutrons were simulated, with nuclear (non-ionizing) and total energy deposition recorded for material thicknesses of 500 μm, 1000 μm, 1500 μm, and 2000 μm. The resulting nuclear and total energy deposition, as a fraction of the nuclear and total energy deposition from all other ions and electrons considered in this analysis for this orbit is shown in Table III. It is observed that the nuclear fractional energy deposition that neutrons contribute dominates the electronic contribution, as one would anticipate. The neutron fraction for this maximum case does not exceed 6% and can be neglected in this analysis because it is eclipsed by the uncertainties in the model spectra themselves. The uncertainty of the trapped radiation models is at best a factor of 2-3 and the solar and GCR models have higher uncertainty, making the errors introduced by neglecting the neutron dose contribution negligible in comparison to the model uncertainty [33].
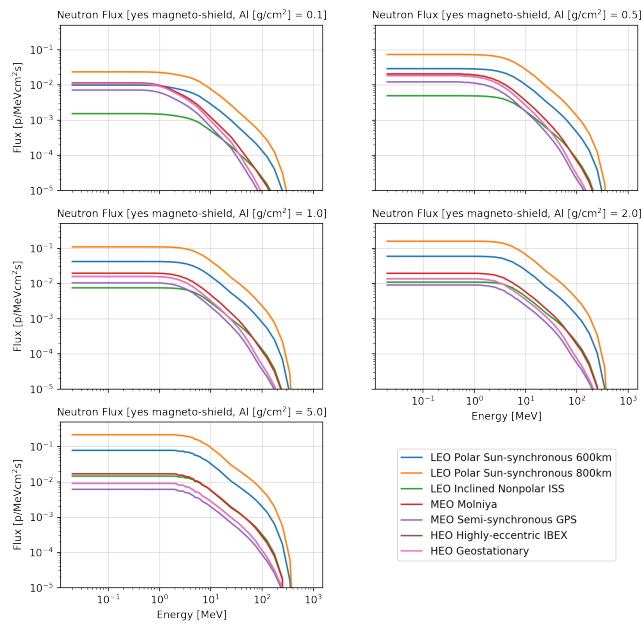
Fig. 10. Neutron spectra produced for all orbit/Al density combinations considered in this analysis. The maximum is shown to be the LEO polar sun-synchronous 800 km orbit with Al thickness of 5.0 g/cm^2.

TABLE III

FRACTION OF NUCLEAR AND TOTAL ENERGY LOSS CONTRIBUTED BY NEUTRONS FOR THE MAXIMUM CASE OF 5.0 G/CM^2 AL SHIELDING AND LEO POLAR SUN-SYNCHRONOUS 800 KM ORBIT WITH MAXIMUM DENSITY MATERIAL ZNTE. THE NEUTRON CONTRIBUTION IS OBSERVED TO NEVER EXCEED 6% FOR THIS MAXIMUM CASE, JUSTIFYING THE EXCLUSION OF NEUTRONS IN THE ANALYSIS, BECAUSE ORBIT RADIATION SPECTRA MODELS HAVE UNCERTAINTIES OF AT BEST A FACTOR OF 2-3 WHICH ECLIPSES THE NEUTRON CONTRIBUTION EFFECT [33].

Thickness [μm]	Neutron Nuclear E_{dep} [%]	Neutron Total E_{dep} [%]
500	5.82%	0.05%
1000	5.73%	0.06%
2000	5.79%	0.06%

APPENDIX D

EFFECT OF SPECTRUM ENERGY BIN DISCRETIZATION

The output spectra of SPENVIS are provided in energy bins, with the flux in units of MeV/cm^{2}s. The effect of the fineness of this discretization is considered here because nuclear and electronic energy loss as a function of distance is calculated bin-wise. To accomplish this, a new energy discretization is defined over the original range with logarithmic interpolation with 10x the number of energy bins. The resulting flux values are sampled through quadratic interpolation. The resulting energy deposited per unit distance for solar He (maximum rate of energy loss for any ion considered in the final analysis) is shown in Fig. 11 for the maximum discretization error orbit: LEO ISS.

The particle with maximum energy loss rate should have the greatest discretization error because the higher energy bins are widest in spacing. For this maximum error orbit, the percentage errors considering 500 μm, 1000 μm, and 2000 μm material thickness are shown in Table IV for nuclear and electronic energy deposition. The maximum error never exceeds 6% and is eclipsed by the minimum factor of 2-3
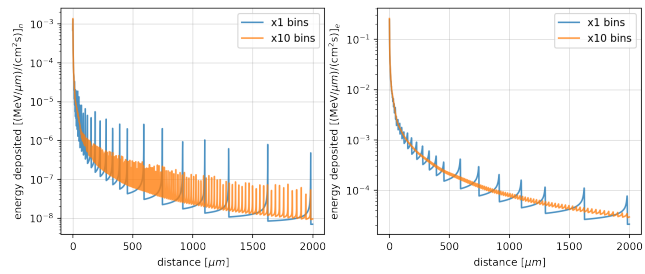

Fig. 11. Nuclear (left) and electronic (right) energy deposited as a function of distance for the maximum discretization error case: Solar He ions in LEO ISS orbit with the number of bins used in the analysis (x1 bins) and an order of magnitude larger number of bins (x10 bins). The resulting percent errors are found in Table IV.

TABLE IV

MAXIMUM FRACTIONAL [%] ERROR IN NUCLEAR AND ELECTRONIC ENERGY LOSS DUE TO DISCRETIZATION (LEO ISS GAN). IT IS OBSERVED THAT THESE ERRORS ARE SUFFICIENTLY SMALL TO BE NEGLECTED BECAUSE ORBIT RADIATION SPECTRA MODELS HAVE UNCERTAINTIES OF AT BEST A FACTOR OF 2-3 WHICH OVERWHELMS THIS BIN DISCRETIZATION EFFECT [33].

Thickness [μm]	Nuclear N_{dep} Error [%]	Electronic N_{dep} Error [%]
500	5.05%	5.31%
1000	5.03%	5.16%
2000	5.02%	5.12%

errors in the flux spectra themselves [33].

REFERENCES

[1] L. Novikov, V. Mileev, E. Voronina, L. Galanina, A. Makletsov, and V. Sinolits, "Radiation effects on spacecraft materials," *J. Surface Investigation. X-ray, Synchrotron and Neutron Tech.*, vol. 3, no. 2, pp. 199–214, April 2009.

[2] D. Sinclair and J. Dyer, "Radiation effects and cots parts in smallsats," *27th Annual AIAA/USU Conf. on Small Satellites*, Aug. 2013, Art. No. SSC13-IV-3.

[3] H. Hughes and J. Benedetto, "Radiation effects and hardening of MOS technology: Devices and circuits," *IEEE Trans. Nucl. Sci.*, vol. 50, pp. 500 – 521, July 2003.

[4] L. Artola, A. A. Youssef, S. Ducret, F. Perrier, R. Buiron, O. Gilard, J. Mekki, M. Boutillier, G. Hubert, and C. Poivey, "Update of single event effects radiation hardness assurance of readout integrated circuit of infrared image sensors at cryogenic temperature," *Sensors*, vol. 18, July 2018, Art. No. s18072338.

[5] E. A. Burke, "Energy dependence of proton-induced displacement damage in Silicon," *IEEE Trans. Nucl. Sci.*, vol. 33, no. 6, pp. 1276–1281, Dec. 1986.

[6] J. H. Warner, S. R. Messenger, R. J. Walters, and G. P. Summers, "Displacement damage correlation of proton and Silicon ion radiation in GaAs," *IEEE Trans. Nucl. Sci.*, vol. 52, no. 6, pp. 2678–2682, Dec. 2005.

[7] S. Messenger, C. Mishler, J. Hack, and P. Dudek, "Characterization of the effects of proton-induced total ionizing dose and displacement damage on the uc1875 controller," in *2019 IEEE Rad. Eff. Data Workshop*, July 2019, pp. 63–67.

[8] A. D. Topper, M. J. Campola, D. Chen, M. C. Casey, K. Yau, D. J. Cochran, K. A. LaBel, R. L. Ladbury, T. K. Mondy, M. V. O'Bryan, J. A. Pellish, E. P. Wilcox, E. J. Wyrwas, and M. A. Xapsos, "Compendium of current total ionizing dose and displacement damage results from NASA goddard space flight center and NASA electronic parts and packaging program," in *2017 IEEE Rad. Eff. Data Workshop*, July 2017, Art. No. 8115431.

[9] M. Alurralde, M. Victoria, A. Caro, and D. Gavillet, "Nuclear and damage effects in Si produced by irradiations with medium energy protons," *IEEE Trans. Nucl. Sci.*, vol. 38, no. 6, pp. 1210–1215, Dec. 1991.

[10] J. C. Bourgoin, J. W. Corbett, and H. L. Frisch, "Ionization enhanced diffusion," *J. Chem. Phys.*, vol. 59, no. 8, pp. 4042–4046, July 1973. [Online]. Available: https://doi.org/10.1063/1.1680596

[11] S. J. Zinkle, "Irradiation spectrum and ionization-induced diffusion effects in ceramics," *MRS Proceedings*, vol. 439, pp. 667–678, Dec. 1996.

[12] W. J. Weber, Y. Zhang, and L. Wang, "Review of dynamic recovery effects on ion irradiation damage in ionic-covalent materials," *Nuc. Instr. and Methods in Phys. Research Sect. B*, vol. 277, pp. 1 – 5, April 2012, basic Research on Ionic-Covalent Materials for Nuclear Applications. [Online]. Available: http://www.sciencedirect.com/science/article/pii/S0168583X11011621

[13] L. Thomé, G. Velisa, S. Miro, A. Debelle, F. Garrido, G. Sattonnay, S. Mylonas, P. Trocellier, and Y. Serruys, "Recovery effects due to the interaction between nuclear and electronic energy losses in sic irradiated with a dual-ion beam," *J. Appl. Phys.*, vol. 117, March 2015, Art. No. 105901.

[14] S. Messenger, C. Mishler, J. Hack, and P. Dudek, "Characterization of the effects of proton-induced total ionizing dose and displacement damage on the uc1708 power driver," in *2018 IEEE Rad. Eff. Data Workshop (REDW)*, July 2018, Art. No. 8584310.

[15] D. J. Cochran, S. D. Kniffin, S. P. Buchner, K. A. LaBel, M. V. O'Bryan, R. L. Ladbury, A. B. Sanders, D. K. Hawkins, S. R. Cox, C. F. Poivey, T. R. Oldham, H. Kim, T. L. Irwin, M. R. Friendlich, A. M. Dung-Phan, M. A. Carts, M. D. Berg, C. M. Seidleck, and J. D. Forney, "Compendium of total ionizing dose results and displacement damage results for candidate spacecraft electronics for NASA," in *IEEE Rad. Eff. Data Workshop*, 2006, pp. 6–12.

[16] M. Treadaway, C. Mallon, T. Flanagan, R. Denson, and E. Wenaas, "The effects of high-energy electrons on the charging of spacecraft dielectrics," *IEEE Trans. Nucl. Sci.*, vol. 26, no. 6, pp. 5101–5106, Dec. 1979.

[17] A. Frederickson, "Electric discharge pulses in irradiated solid dielectrics in space," *IEEE Trans. Elect. Insul.*, no. 3, pp. 337–349, June 1983.

[18] J. R. Srour, C. J. Marshall, and P. W. Marshall, "Review of displacement damage effects in Silicon devices," *IEEE Trans. Nucl. Sci.*, vol. 50, no. 3, pp. 653–670, July 2003.

[19] J. R. Srour and J. W. Palko, "Displacement damage effects in irradiated semiconductor devices," *IEEE Trans. Nucl. Sci.*, vol. 60, no. 3, pp. 1740–1766, June 2013.

[20] "NSRL user guide," Accessed on: July 25, 2020. [Online]. Available: https://www.bnl.gov/nsrl/userguide/beam-ion-species-and-energies.php

[21] "88-inch cyclotron," Accessed on: July 25, 2020. [Online]. Available: http://cyclotron.lbl.gov/

[22] J. D. Bergeson, R. Bommena, S. Fahey, V. M. Cowan, C. P. Morath, and S. Velicu, "Mid and long wavelength infrared HgCdTe photodetectors exposed to proton radiation," in *Proc. SPIE*, vol. 9926, Sept. 2014, Art. No. 99260P.

[23] V. M. Cowan, C. P. Morath, J. E. Hubbs, S. Myers, E. Plis, and S. Krishna, "Radiation tolerance characterization of dual band InAs/GaSb type-II strain-layer superlattice pBp detectors using 63 MeV protons," *Appl. Phys. Lett.*, vol. 101, Dec. 2012, Art. No. 251108.

[24] S. Fahey, S. Velicu, R. Bommena, J. Zhao, V. M. Cowan, C. P. Morath, and S. Sivananthan, "Proton irradiation of MWIR HgCdTe/CdZnTe," in *Proc. SPIE*, vol. 9616, Sept. 2015, Art. No. 96160E-1.

[25] L. Hoglund, D. Ting, A. Khoshakhlagh, A. Soibel, A. Fisher, C. Hill, S. Keo, S. Rafol, and S. Gunapala, "Influence of proton radiation on the minority carrier lifetime in midwave InAs/InAsSb superlattices," *Appl. Phys. Lett.*, vol. 108, no. 2, July 2016, Art. No. 263504.

[26] J. Hubbs, M. Gramer, D. Arrington, G. Dole, D. Maestas-Jepson, and S. Takeall, "Total ionizing dose and proton radiation characterization of Si p-i-n visible hybrid focal plane arrays," in *Proc. SPIE*, vol. 5902, June 2005, Art. No. 59020M.

[27] J. E. Hubbs, P. W. Marshall, C. J. Marshall, M. E. Gramer, D. Maestas, J. P. Garcia, G. A. Dole, and A. A. Anderson, "Lateral diffusion length changes in HgCdTe detectors in a proton environment," *IEEE Trans. Nucl. Sci.*, vol. 54, no. 6, pp. 2435–2443, Dec. 2007.

[28] J. Hubbs, "Proton radiation experimental results on a III-V nbn mid-wavelength infrared focal plane array," in *Proc. SPIE*, Sept. 2016, Art. No. 9933.

[29] G. D. Jenkins, C. P. Morath, and V. M. Cowan, "Emperical trends of minority carrier recombination lifetime vs proton radiation for rad-hard IR detector materials," in *Proc. SPIE*, vol. 9616, Dec. 2015, Art. No. 96160G1-9.

[30] C. P. Morath, V. M. Cowan, L. A. Treider, G. D. Jenkins, and J. E. Hubbs, "Proton irradiation effects on the performance of III-V-based, unipolar barrier infrared detectors," *IEEE Trans. Nucl. Sci.*, vol. 62, no. 2, pp. 512–519, Feb. 2015.

[31] C. P. Morath, E. A. Garduno, G. D. Jenkins, and V. M. Cowan, "More accurate quantum efficiency damage factor for proton-irradiated, III-

V-based unipolar barrier infrared detectors," *IEEE Trans. Nucl. Sci.*, vol. 64, no. 1, pp. 74–80, Dec. 2017.

[32] E. Steenbergen, J. A. Massengale, V. M. Cowan, Z. Lin, Y.-H. Zhang, and C. P. Morath, "Proton radiation effects on the photoluminescence of infrared InAs/InAsSb superlattices," in *Proc. SPIE*, Sept. 2013, Art. No. 887601.

[33] H. Evans, "Space environment basics and calculation methods," *ESA Internal Course EEE Component Rad. Hardness Assurance Tutorial*, Nov. 2016, Accessed on: July 25, 2020. [Online]. Available: https://indico.cern.ch/event/635099/contributions/2570659/attachments/1456183/2249867/2_Radiation_Effects_and_RHA_ESA_Internal_Course_9_May_space_environment_HE.pdf

[34] *AU-18 Space Primer*. Air Command and Staff College, DTIC, Oct. 2011, Accessed on: July 25, 2020. [Online]. Available: https://www.airuniversity.af.edu/Portals/10/AUPress/Books/AU-18.PDF

[35] L. Policastri, J. Carrico, and R. Lebois, "Flight dynamics operations for the IBEX mission: The first six months," *AAS/AIAA Astrodynamics Specialist Conf.*, Aug. 2009, Art. No. 09-350.

[36] *SPace ENVironment Information System (SPENVIS)*, 08 2019, Accessed on: July 25, 2020. [Online]. Available: https://www.spenvis.oma.be/intro.php

[37] S. Q. Kidder and T. H. Vonder Haar, "On the use of satellites in Molniya orbits for meteorological observation of middle and high latitudes," *J. Atmospheric and Oceanic Tech.*, vol. 7, no. 3, pp. 517–522, June 1990. [Online]. Available: https://doi.org/10.1175/1520-0426(1990)007⟨0517:OTUOSI⟩2.0.CO;2

[38] B. Riddle, "Beyond earth's orbit," *Science Scope*, vol. 40, no. 7, March 2017, Art. No. 24.

[39] M. A. Xapsos, C. Stauffer, T. Jordan, J. L. Barth, and R. A. Mewaldt, "Model for cumulative solar heavy ion energy and linear energy transfer spectra," *IEEE Trans. Nucl. Sci.*, vol. 54, no. 6, pp. 1985–1989, Dec. 2007.

[40] M. J. Boschini, P. G. Rancoita, and M. Tacconi, "Screened relativistic (sr) nuclear stopping power calculator," 2014, Accessed on: July 25, 2020. [Online]. Available: http://www.sr-niel.org

[41] C. Leroy and P.-G. Rancoita, *Principles Of Radiation Interaction In Matter And Detection (4th Edition)*. World Sci. Pub. Co., Dec. 2015. [Online]. Available: https://books.google.com/books?id=Km_FCwAAQBAJ

[42] J. F. Ziegler, "SRIM - the stopping and range of ions in matter," 2013, Accessed on: July 25, 2020. [Online]. Available: http://www.srim.org/

[43] M. J. Berger, J. S. Zucker, and J. Chang, "Standard reference database 124," July 2017, Accessed on: July 25, 2020. [Online]. Available: https://www.nist.gov/pml/stopping-power-range-tables-electrons-protons-and-helium-ions

[44] D. M. Sawyer and J. I. Vette, "AP-8 trapped proton environment for solar maximum and solar minimum," NASA STI/Recon Technical Rep. 18983, Dec. 1976, Accessed on: July 25, 2020.

[45] J. Vette, *The AE-8 Trapped Electron Model Environment*, ser. NSSDC/WDC-A-R & S. Nat. Space Sci. Data Center (NSSDC), World Data Center A for Rockets and Satellites (WDC-A-R&S), Nat. Aeronautics and Space Adm., Goddard Space Flight Ctr., Nov. 1991.

[46] M. A. Xapsos, G. P. Summers, J. L. Barth, E. G. Stassinopoulos, and E. A. Burke, "Probability model for cumulative solar proton event fluences," *IEEE Trans. Nucl. Sci.*, vol. 47, no. 3, pp. 486–490, Sept. 2000.

[47] D. Matthiä, T. Berger, A. I. Mrigakshi, and G. Reitz, "A ready-to-use galactic cosmic ray model," *Adv. in Space Research*, vol. 51, no. 3, pp. 329–338, Feb. 2013.

[48] J. V. Logan, M. P. Short, P. T. Webster, C. P. Morath, and E. H. Steenbergen, "Impact of proton-induced transmutation doping in semiconductors for space applications," *J. Mater. Chem. C*, vol. 7, pp. 8905–8914, June 2019. [Online]. Available: http://dx.doi.org/10.1039/C9TC02995H

[49] T. E. Dutton, W. F. Woodward, and T. S. Lomheim, "Simulation of proton-induced transients on visible and infrared focal plane arrays in a space environment," in *Infrared Imaging Systems: Design, Analysis, Modeling, and Testing VIII*, G. C. Holst, Ed., vol. 3063, Int. Society for Optics and Photonics. SPIE, June 1997, pp. 77 – 101. [Online]. Available: https://doi.org/10.1117/12.276088

[50] J. V. Logan and M. P. Short, June 2020, Accessed on: July 25, 2020. [Online]. Available: shortlab/TestOrbitDurationEquivalence_2020:2020

[51] F. Ravotti, "Dosimetry techniques and radiation test facilities for total ionizing dose testing," *IEEE Trans. Nucl. Sci.*, vol. 65, no. 8, pp. 1440–1464, April 2018.